

Li₁₅P₄S₁₆Cl₃, a Lithium Chlorothiophosphate as a Solid-State Ionic Conductor

Z. Liu, J. Bai

To be published in "INORGANIC CHEMISTRY"

January 2020

Photon Sciences

Brookhaven National Laboratory

U.S. Department of Energy

USDOE Office of Science (SC), Basic Energy Sciences (BES) (SC-22)

Notice: This manuscript has been authored by employees of Brookhaven Science Associates, LLC under Contract No. DE-SC0012704 with the U.S. Department of Energy. The publisher by accepting the manuscript for publication acknowledges that the United States Government retains a non-exclusive, paid-up, irrevocable, world-wide license to publish or reproduce the published form of this manuscript, or allow others to do so, for United States Government purposes.

DISCLAIMER

This report was prepared as an account of work sponsored by an agency of the United States Government. Neither the United States Government nor any agency thereof, nor any of their employees, nor any of their contractors, subcontractors, or their employees, makes any warranty, express or implied, or assumes any legal liability or responsibility for the accuracy, completeness, or any third party's use or the results of such use of any information, apparatus, product, or process disclosed, or represents that its use would not infringe privately owned rights. Reference herein to any specific commercial product, process, or service by trade name, trademark, manufacturer, or otherwise, does not necessarily constitute or imply its endorsement, recommendation, or favoring by the United States Government or any agency thereof or its contractors or subcontractors. The views and opinions of authors expressed herein do not necessarily state or reflect those of the United States Government or any agency thereof.

Li₁₅P₄S₁₆Cl₃, a new lithium chloro-thiophosphate as a solid-state ionic conductor

Zhantao Liu¹, Tatiana Zinkevich², Sylvio Indris², Xingfeng He³, Jue Liu⁴, Wenqian Xu⁵, Jianming Bai⁶, Shan Xiong¹, Yifei Mo³, Hailong Chen^{1*}

¹ *The Woodruff School of Mechanical Engineering, Georgia Institute of Technology, Atlanta, GA, 30332, USA*

² *Institute for Applied Materials, Karlsruhe Institute of Technology, Hermann-von-Helmholtz Platz 1, D-76344 Eggenstein-Leopoldshafen, Germany*

³ *Department of Materials Science and Engineering, University of Maryland, College Park, Maryland 20742, USA*

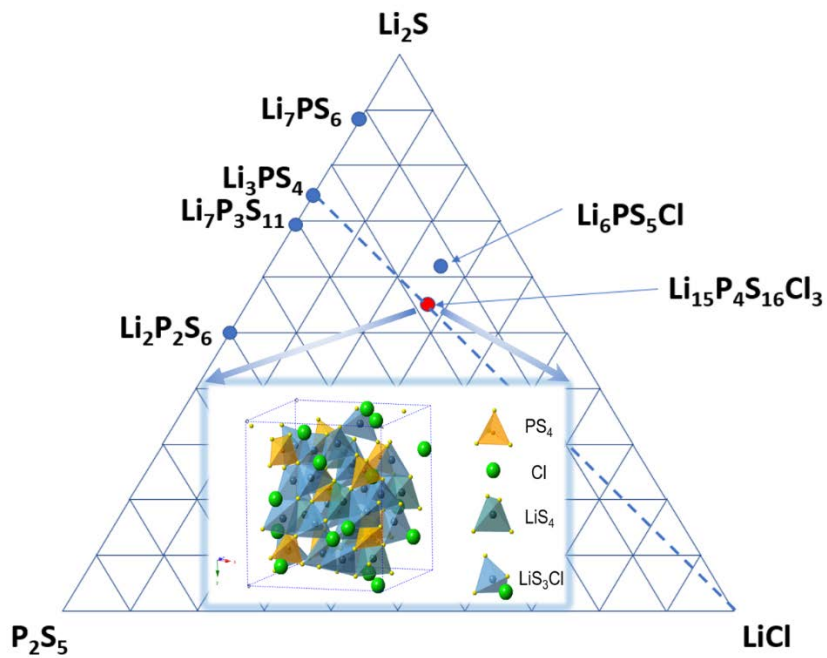
⁴ *Neutron Scattering Division, Oak Ridge National Laboratory, Oak Ridge, Tennessee 37831, United States*

⁵ *X-ray Science Division, Advanced Photon Source, Argonne National laboratory, Argonne, Illinois 60439, United States*

⁶ *National Synchrotron Light Source II, Brookhaven National Laboratory, Upton, New York 11973, United States*

Correspondence should be addressed to Hailong Chen via E-mail address: hailong.chen@me.gatech.edu

TOC



Synopsis

A novel lithium chloro-thiophosphate $\text{Li}_{15}\text{P}_4\text{S}_{16}\text{Cl}_3$ was found in Li_2S - P_2S_5 - LiCl phase diagram and synthesized. Synchrotron X-ray Diffraction and Neutron Diffraction techniques were used to clarify the crystal structure. The lithium dynamics was studied by electrochemical impedance spectroscopy, solid state NMR technique and theoretical calculation.

Abstract

Tremendous efforts have been devoted to the design of solid Li⁺ electrolytes and development of all-solid-state batteries. Compared with conventional Li-ion batteries which use flammable liquid organic electrolytes, all-solid-state batteries show significant advantages in safety. In this work a novel lithium chloro-thiophosphate compound Li₁₅P₄S₁₆Cl₃ is discovered. The crystal structure and electrochemical properties are investigated. Li₁₅P₄S₁₆Cl₃ can be synthesized as pure phase via a facile solid-state reaction by heating ball-milled mixture of Li₂S, P₂S₅ and LiCl at 360 °C. The crystal structure of Li₁₅P₄S₁₆Cl₃ was refined against neutron and synchrotron X-ray powder diffraction data, revealing that it crystallizes in space group $I\bar{4}3d$. The Li⁺ transport in Li₁₅P₄S₁₆Cl₃ was also investigated by multiple solid state NMR methods, including variable-temperature NMR lineshape analysis, NMR relaxometry, and pulsed field-gradient NMR. Li₁₅P₄S₁₆Cl₃ shows good thermodynamic stability and can be synthesized at relatively low temperature. Though it exhibits a low ionic conductivity at room temperature, it can serve as a new motif crystal structure for the design and development of new solid state electrolytes.

Introduction

All-solid-state Li-ion batteries (ALSOLIBs) are considered an emerging battery technology for next generation electrochemical energy storage. Currently used commercial Li-ion batteries (LIBs) contain flammable organic electrolytes, which may cause fire or explosion in harsh or abusive environments. Compared with commercial LIBs, ALSOLIBs with non-flammable solid electrolyte (SEs) not only have much better safety properties, but also potentially have higher energy density, if Li-metal anode can be enabled¹⁻⁴.

As the key component of ALSOLIB, the SE must meet the requirements in multiple categories of properties, including high ionic conductivity at ambient temperature, good chemical and electrochemical stability and good mechanical durability, etc. Commonly, SEs with room temperature (r.t.) ionic conductivity higher than 10^{-4} S cm⁻¹ are preferred⁵⁻⁶. To date, predominantly two groups of SEs have attracted much attentions: sulfide-based and oxide-based electrolytes. Oxide electrolytes, such as compounds with perovskite, NASICON or garnet structures, exhibit r.t. ionic conductivity from 10^{-5} to 10^{-3} S cm⁻¹⁷⁻⁹. However, large grain boundary (GB) resistance was often observed because of the poor electrical contact among the particles. High temperature sintering may help to mitigate the GB resistance, which significantly increases the complexity and cost of the manufacturing process¹⁰⁻¹² and may result in unwanted side reactions with the cathode materials¹³⁻¹⁴. In contrast, sulfide SEs are soft and ductile. Good electrical contact among the particles and thus low GB resistance can be relatively easily achieved by facile cold-pressing¹⁵. A number of lithium sulfides with high r.t. ionic conductivities reaching or even exceeding 10^{-3} S cm⁻¹ have been reported¹⁶⁻¹⁸, including Li₃PS₄-Li₄GeS₄ solid solutions with LISICON structure¹⁹, Li₆PS₅X (X=Cl, Br, I) with argyrodite structure²⁰⁻²³, Li₇P₃S₁₁ glass ceramics²⁴, and Li₁₀GeP₂S₁₂ (LGPS)²⁵, etc. Some of these SEs,

such as LGPS, exhibit very high r. t. ionic conductivity of 10^{-2} S cm⁻¹, which exceeds that of liquid electrolytes²⁶, demonstrating the great potential of sulfide SEs. However, most of these known sulfide SEs require sophisticated processing (such as long time, high speed ball-milling and precise control of starting materials) and high temperature (>500°C) synthesis to achieve the expected high conductivities¹⁷. SEs with not only high r.t. conductivity, but also facile and low cost synthesis, are still very much desired. From crystal structure point of view, all these known sulfide SEs only present a few limited types of crystal structures. Most of current designs and developments of SEs are focused on the elementary modifications based on these known structure types, which can be limited sometimes. Addition of new crystal structure motifs is also desired. Compared with the relatively extensively explored Li-P-S ternary phase diagram, the quaternary phase diagrams of Li-P-S-X (X=halogen elements) are much less explored, which provides high potential to find new prototypes of Li-ion conducting crystal structures. For example, Li₄PS₄I was recently reported and its ionic conductivity is 1.2×10^{-4} S/cm⁶. One group of Li-P-S-X compounds, the argyrodites Li₆PS₅X (X=Cl, Br, I), recently attracted a lot of attentions owing to their high conductivities^{5, 21, 27-28}, demonstrating high potential of these quaternary compounds. Besides the argyrodites, no other Li-P-S-X quaternary compounds have been reported and a large area in the phase diagram remains unexplored. Recent computational works predicted that Li₁₅P₄S₁₆Cl₃²⁹⁻³⁰, can be thermodynamically stable. But no synthesis condition and crystal structure information was disclosed to date. Here we successfully synthesized a new compound Li₁₅P₄S₁₆Cl₃ with a new crystal structure distinguished from all known sulfide SEs. The structural characterizations and ionic conduction behaviors of the compound are elaborated below.

Methods

Materials synthesis

$\text{Li}_{15}\text{P}_4\text{S}_{16}\text{Cl}_3$ was synthesized via a ball-milling and subsequent calcination process. The starting materials Li_2S (99.98%, Sigma-Aldrich), P_2S_5 (99%, Sigma-Aldrich) and LiCl (>99%, Sigma-Aldrich) were weighed in desired molar ratio and mixed in a high energy planetary ball mill (PM 200, Retsch) with using a zirconia jar. 10 zirconia balls of 10 mm diameter were put in each jar. The starting materials are ball-milled for 20 h at a rotation speed of 370 rpm. The ball-milled mixture was then pressed into pellets of ½ inch in diameter and sealed in a quartz tube. The pellets were heated at 360 °C for 20 h and cooled down inside the furnace. The pellets were ground into powder in an agate mortar and kept in an Ar gas filled glove box for the following characterizations. All materials were handled under Argon atmosphere during the synthesis, characterization and electrochemical testing processes.

Characterizations

The X-ray diffraction (XRD) data of the powder samples was first collected by using a D8 Advance X-ray Diffractometer (Bruker AXS) with molybdenum radiation ($\lambda_{\text{K}\alpha 1} = 0.7093 \text{ \AA}$). *In situ* XRD data of the synthesis process was also collected with using a heat chamber (HTK1200N, Anton Paar) mounted on the diffractometer as follows. The powder of ball-milled mixture of starting materials was filled in quartz capillary in the glove box and sealed. The tube was used for in situ XRD data collection and heated from room temperature to 440 °C.. XRD data were collected in a step size of 20 °C while the temperature was kept constant during each XRD scan.

Synchrotron XRD and pair distribution function (PDF) data were collected at beam line 17-BM-B at the Advanced Photon Source (APS) at Argonne National Laboratory (ANL), with a wavelength of 0.24116 Å. High quality powder neutron diffraction (ND) data were collected on beam line POWGEN at the Spallation Neutron Source (SNS) at Oak Ridge National Laboratory (ORNL) using the frame with a center wavelength of 0.8 Å. Rietveld refinement against the XRD and ND data was performed with using GSAS II and TOPAS (version 6) software³¹⁻³². The conversion from time-of-flight to d-spacing was done using a 2nd order polynomial function ($\text{TOF} = d_0 + d_{fc} * d + d_{fa} * d^2$) calibrated from a NIST Si 640e standard sample. During the refinement, d_0 and d_{fc} were fixed to the values refined from Si standard while d_{fa} was allowed to vary to account for the sample displacement. The crystal structure model obtained from the Rietveld refinement was used as the starting model for the analysis of PDF data. The X-ray PDF data was processed with using PDFgetX3³³. The total scattering structure factor $S(Q)$ data were Fourier transformed to the PDF with a maximum Q -range (Q_{max}) of 19 Å⁻¹. The collected data were corrected for background and sample absorption. PDFgui and TOPAS (version 6) were used for the PDF data analysis^{32, 34}.

Scanning Electron Microscopy (SEM) images were taken by using a Hitachi SU8010 scanning electron microscope. The sample was transferred from the glove box in well-sealed container to minimize the air exposure.

⁶Li and ³¹P magic-angle spinning (MAS) NMR spectroscopy was performed with a Bruker Avance 500 MHz spectrometer. The magnetic field of 11.7 T corresponds to Larmor frequencies of 73.6 for ⁶Li and 202.5 MHz for ³¹P. The samples were rotated in 2.5 mm zirconia rotors at a spinning speed of 20 kHz. All spectra were acquired with a Hahn-echo pulse sequence³⁵. The

chemical shifts were referenced to an aqueous 1M ${}^6\text{LiCl}$ solution for ${}^6\text{Li}$ and to H_3PO_4 (85%) for ${}^{31}\text{P}$.

Temperature-dependent measurements of static ${}^7\text{Li}$ NMR line shapes and ${}^7\text{Li}$ spin–lattice relaxation times were performed with a Bruker 200 MHz spectrometer at a magnetic field of 4.7 T, on samples sealed in 10 mm glass vials. These spectra were acquired with a quadrupolar-echo sequence, a $\pi/2$ pulse length of about 3 μs , and a recycle delay of 20 s. ${}^7\text{Li}$ T_1 measurements were performed with a saturation-recovery pulse sequence³⁶⁻³⁷. ${}^7\text{Li}$ pulsed field-gradient (PFG) NMR measurements were acquired with a stimulated-echo sequence including bipolar gradients, on a Bruker Avance 300 MHz spectrometer operated with a Diff50 probe that provides pulsed field gradients up to 30 T/m³⁸.

***Ab initio* molecular dynamic simulations**

Density functional theory (DFT) calculations were conducted with using the Vienna *Ab initio* Simulation package (VASP)³⁹ within the projector augmented-wave approach with Perdew-Burke-Ernzerhof (PBE)⁴⁰ generalized-gradient approximation (GGA). *Ab initio* molecular dynamic (AIMD) simulations were performed to investigate Li diffusion. A Γ -centered k -point in the non-spin-polarized DFT calculations were used. The time step was 2 fs. NVT ensemble using Nosé-Hoover thermostat⁴¹ was used. The total time of AIMD simulations were in the range of 100 ps to 600 ps. The ionic conductivity and the error bars were calculated and estimated following previously established methods⁴².

Electrochemical measurements

Ionic conductivity was determined by electrochemical impedance spectroscopy (EIS) method by an electrochemical impedance analyzer (VMP3, Bio-Logic) and a custom-built electrochemical cell. Typically, ~130 mg $\text{Li}_{15}\text{P}_4\text{S}_{16}\text{Cl}_3$ powder was pressed into a pellet with a diameter of $\frac{1}{2}$ inch at a pressure of 100 bars. Two stainless steel rods were used as the current collectors. EIS data were collected in the temperature range of 30 °C to 90 °C at frequencies between 1MHz and 1Hz and with AC amplitude of 500 mV.

Results and discussion

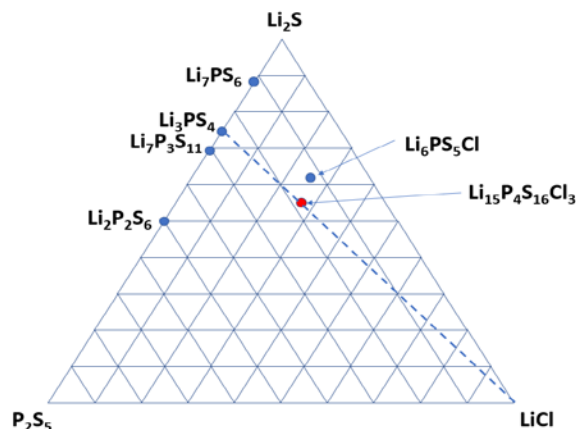


Fig. 1. Li-P-S-Cl quaternary phase diagram plotted in Li₂S-P₂S₅-LiCl ternary manner.

The quaternary Li-P-S-Cl phase diagram can be plotted in an equivalent Li₂S-P₂S₅-LiCl ternary phase diagram with better clarity, as shown in Fig. 1. The argyrodite Li₆PS₅Cl is the only known phase in the middle of the phase diagram but it is very unlikely that it is the only phase. In this phase diagram, Li₂S, LiCl, P₂S₅ and Li₃PS₄ are considered thermodynamically stable, while Li₇P₃S₁₁⁴³, Li₇PS₆⁴⁴ and Li₆PS₅Cl⁴⁵ were predicted to be metastable in static DFT calculations at 0K. Previous studies showed that the formation energy of Li₁₅P₄S₁₆Cl₃ is 8 meV/atom, indicating Li₁₅P₄S₁₆Cl₃ is just slightly metastable in the relevant Li-P-S-Cl phase diagram²⁹ similar to Li₇P₃S₁₁⁴³, Li₇PS₆⁴⁴ and Li₆PS₅Cl⁴⁵. The formation energy of Li₁₅P₄S₁₆Cl₃ from the precursor phases, Li₂S, P₂S₅ and LiCl is -3.203 eV/atom, indicating it is energetically favorable formation during synthesis. Therefore, we conducted a systematical exploration on selected regions of the phase diagram with the help of in situ XRD for synthesis. The lithium-rich region on the top right area of the phase diagram was first explored and one new phase was quickly identified. In situ XRD on the solid state synthesis of starting materials with various materials ratios were performed. Fig. 2 shows the in situ XRD patterns collected from the starting materials with ratio of Li₂S: P₂S₅: LiCl = 3:1:1.5. The sample was heated from room

temperature to 450 °C. The diffraction pattern at 50 °C shows the amorphous characteristics of the ball-milled mixture and diffraction peaks with relative low intensity, which can be indexed using minor phases Li_2S and LiCl . As the temperature increases, the intensity of these peaks increases, indicating the increase of crystallinity of Li_2S and LiCl . Once the temperature reaches 150 °C, the reflections associated with the Li_2S phase start to diminish, which is accompanied by the appearance of reflections

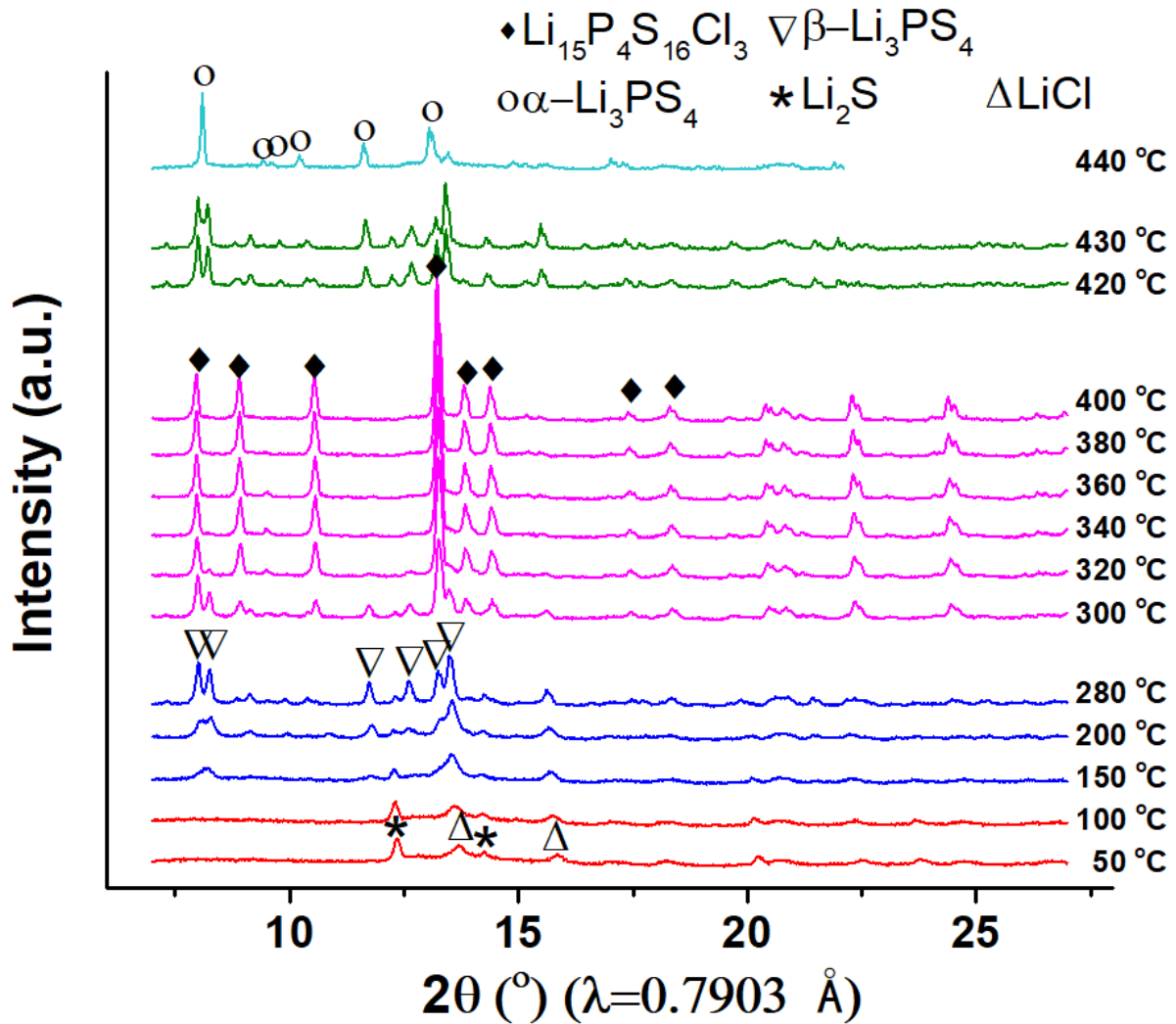


Fig. 2. In situ XRD patterns of ball-milled starting materials Li_2S , P_2S_5 , and LiCl with a molar ratio of 3:1:1.5, heated from 50 to 440 °C.

belonging to the β - Li_3PS_4 phase. At 300 °C, a new set of reflections emerge, which cannot be indexed to commonly known lithium thiophosphate compound. Meanwhile, the intensity of reflections associated with β - Li_3PS_4 and LiCl phases start to decrease, implying that a new phase

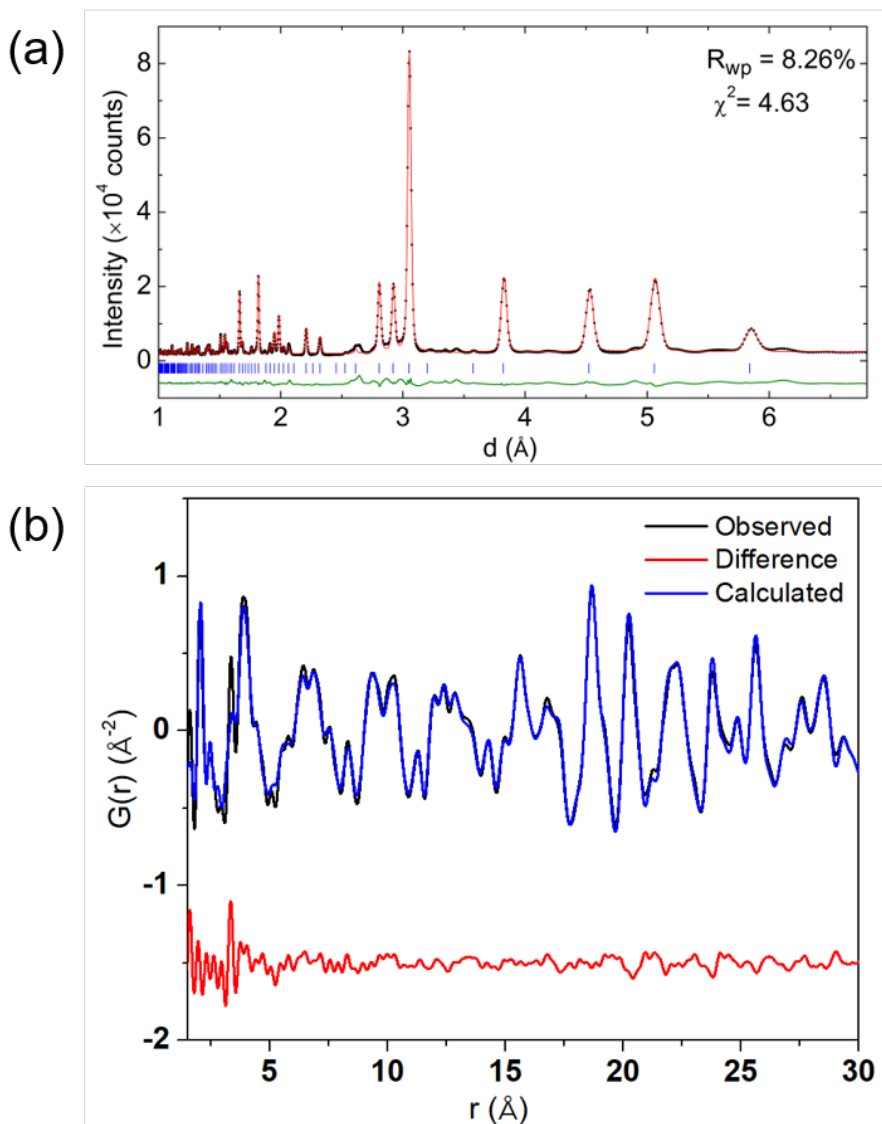


Fig. 3. (a) Rietveld refinement of the long range structure of $\text{Li}_{15}\text{P}_4\text{S}_{16}\text{Cl}_3$ against synchrotron X-ray diffraction data ($\lambda=0.24116$ \AA). (b) Least square refinement of the intermediate range structure of $\text{Li}_{15}\text{P}_4\text{S}_{16}\text{Cl}_3$ with using synchrotron X-ray PDF data.

forms from the reaction between $\beta\text{-Li}_3\text{PS}_4$ and LiCl . The mixture is fully converted into the new phase at $340\text{ }^\circ\text{C}$, where no more reflections from $\beta\text{-Li}_3\text{PS}_4$ and LiCl can be seen. The new phase is stable up to $400\text{ }^\circ\text{C}$ and decomposes to $\beta\text{-Li}_3\text{PS}_4$ and LiCl at $420\text{ }^\circ\text{C}$. $\beta\text{-Li}_3\text{PS}_4$ turns into $\alpha\text{-Li}_3\text{PS}_4$ above $440\text{ }^\circ\text{C}$.

Since no other phases were seen at $360\text{ }^\circ\text{C}$, it can be assumed that all starting materials were converted into this new phase. Therefore, the ratio of the elements in this new phase is $\text{Li}:\text{P}:\text{S}:\text{Cl} = 15:4:16:3$, and the formation reaction can be written as follows:

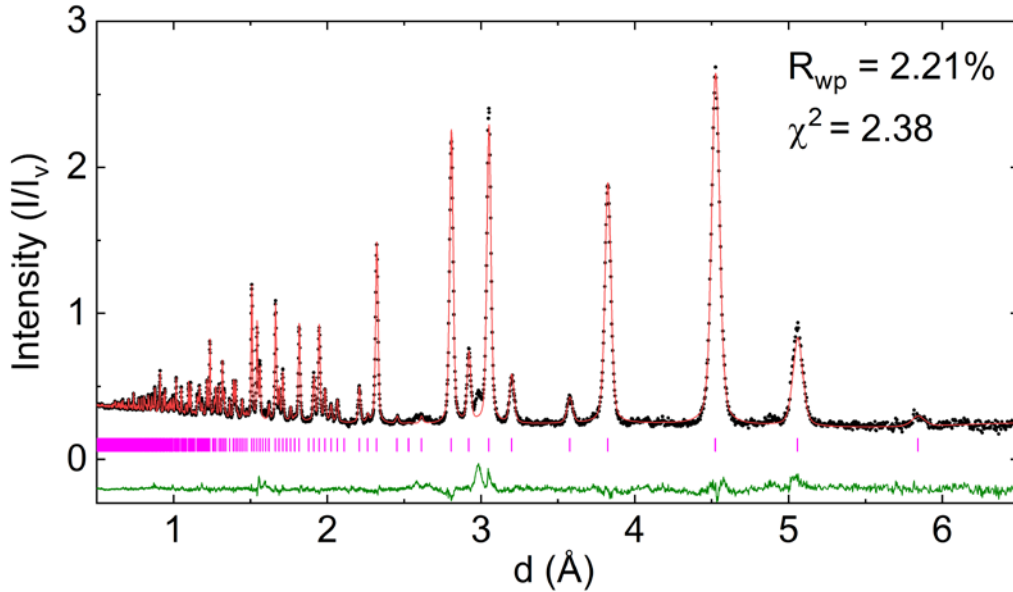
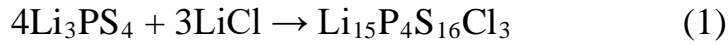


Fig. 4. Rietveld refinement of $\text{Li}_{15}\text{P}_4\text{S}_{16}\text{Cl}_3$ against time-of-flight neutron diffraction data (POWGEN). The experiment data are shown in black dots, calculated data in red curve and difference curve in olive. The Bragg reflections are shown in blue markers. There is one unidentified peak around 3 \AA , indicating the co-existence of impurity phase(s).

$\text{Li}_{15}\text{P}_4\text{S}_{16}\text{Cl}_3$ is a new composition that has not been reported on its detailed crystal structure. However, its silver analogue $\text{Ag}_{15}\text{P}_4\text{S}_{16}\text{Cl}_3$ does exist and its XRD pattern very much resembles the pattern observed in Fig. 2. Given the similarity in charge and ionic radius of Ag^+ and Li^+ , the similar XRD patterns strongly imply that the actual elementary composition of the new phase is likely $\text{Li}_{15}\text{P}_4\text{S}_{16}\text{Cl}_3$. To verify this assumption, high resolution powder synchrotron XRD data was collected and Rietveld refinement of the structure was performed using the space group of $\text{Ag}_{15}\text{P}_4\text{S}_{16}\text{Cl}_3$ as the starting model, but with all Ag atoms replaced by Li atoms. Fig. 3 shows the refinement result using the $\bar{1}43d$ space group. A high quality fitting with a R_{wp} value of 8.26% was achieved, confirming that this new compound indeed has similar structure as the $\text{Ag}_{15}\text{P}_4\text{S}_{16}\text{Cl}_3$. This has been further confirmed by the good quality refinement of the intermediate range structure using X-ray PDF ($R_{\text{w}}=18.6\%$). The minor discrepancy in the low r -range may result from a small amount of amorphous phase, as reported before⁴⁶⁻⁴⁷.

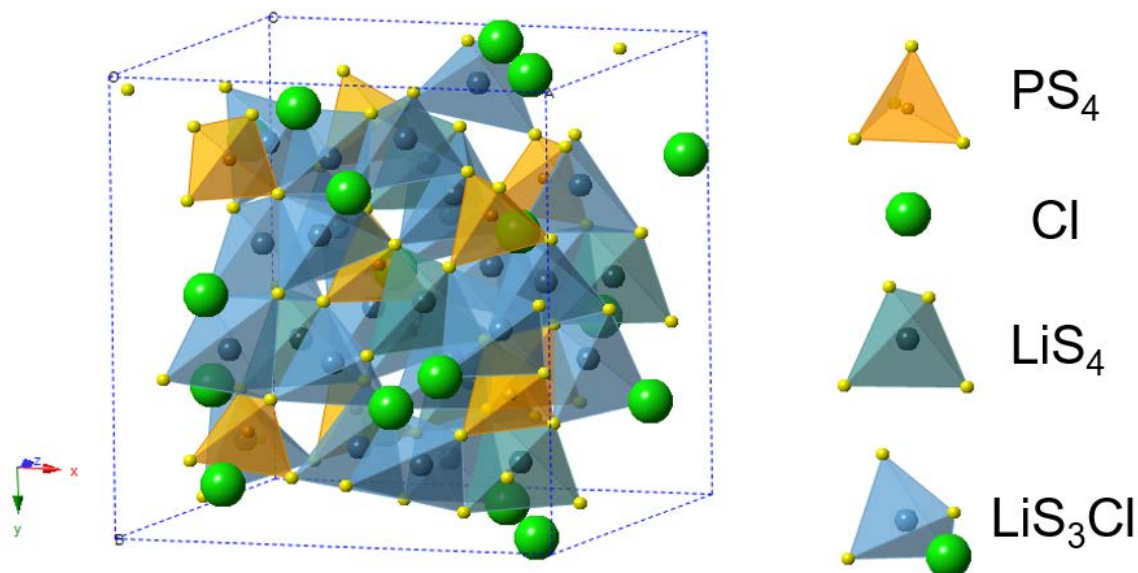


Fig. 5. Refined crystal structure of $\text{Li}_{15}\text{P}_4\text{S}_{16}\text{Cl}_3$ using neutron powder diffraction data.

The Li positions were further confirmed with using Fourier difference map analysis of both neutron and synchrotron X-ray powder diffraction data, as shown in Figure S1 in the supplementary information. It clearly indicates the two plausible Li sites, which matches well those Li positions obtained from Rietveld refinements.

The final Rietveld refinement of the crystal structure of $\text{Li}_{15}\text{P}_4\text{S}_{16}\text{Cl}_3$ against neutron diffraction data is shown in Fig. 4. The refined cell parameter a of $14.3052(3) \text{ \AA}$ is smaller than that of $\text{Ag}_{15}\text{P}_4\text{S}_{16}\text{Cl}_3$ ($a=14.838 \text{ \AA}$)⁴⁸, in accordance with that Li^+ has smaller ionic radii (0.59 \AA , four coordinated) relative to Ag^+ (1.00 \AA , four coordinated)⁴⁹. The crystallographic information extracted from neutron diffraction data is listed in Table 1. The crystal structure drawn based on the refinement result is shown in Fig. 5. The structure is built by three kinds of tetrahedra: PS_4 , LiS_4 and $\text{Li}(\text{S}_3\text{Cl})$. All tetrahedra are connected via common corners. Every S or Cl atom is corner shared by 4 tetrahedra. Li atoms occupy two different tetrahedral sites: $\text{Li}(1)$ occupies the $12a$ site and is bonded to four S^{2-} ions; while $\text{Li}(2)$ occupies the $48e$ site and is bonded to three S^{2-} and one Cl^- .

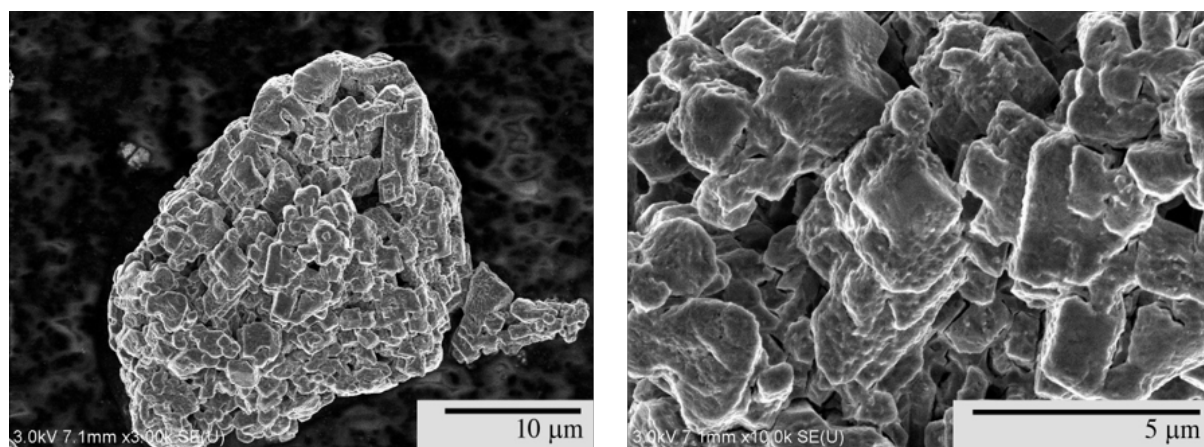


Fig. 6. SEM images of $\text{Li}_{15}\text{P}_4\text{S}_{16}\text{Cl}_3$

SEM images of as synthesized $\text{Li}_{15}\text{P}_4\text{S}_{16}\text{Cl}_3$ are shown in Fig. 6. The primary particles with a dimension ranging from 1 to 5 μm are of cubic/cuboid shapes, in accordance with its space group symmetry. The primary particles are agglomerated to form secondary particles of a few tens micrometers, which is likely due to the fact that the sample was cooled down from a molten phase.

Table 1. Refined structure of $\text{Li}_{15}\text{P}_4\text{S}_{16}\text{Cl}_3$ using neutron diffraction data.

| S.G. <i>I</i> -43d $a = 14.3052(3) \text{ \AA}$ | | | | | | |
|---|-------|-----------|-----------|-----------|------|---------------------------------|
| Site | Wyck. | x | y | z | Occ. | $B_{\text{iso}} (\text{\AA}^2)$ |
| Li(1) | 12a | 0.00000 | 0.25000 | 0.37500 | 1 | 1.85(7) |
| Li(2) | 48e | 0.1420(3) | 0.2145(3) | 0.5825(4) | 1 | 1.85(7) |
| S(1) | 16c | 0.0320(2) | 0.0320(2) | 0.0320(2) | 1 | 1.09(4) |
| S(2) | 48e | 0.1080(2) | 0.3433(2) | 0.4713(2) | 1 | 1.09(4) |
| Cl(1) | 12b | 0.00000 | 0.25000 | 0.87500 | 1 | 1.71(4) |
| P(1) | 16c | 0.1997(1) | 0.1997(1) | 0.1997(1) | 1 | 0.90(4) |

The local structure around the Li and the P ions was investigated by ^6Li and ^{31}P MAS NMR spectroscopy, respectively. The spectra are shown in Fig. 7. The ^6Li NMR spectrum (Fig. 7a) reveals two well-resolved narrow peaks. The stronger one at 1.0 ppm can be assigned to the Li(2) site at 48*e* position, and the weaker peak is assigned to the Li(1) site at 12*a* position. The ^{31}P spectrum (Fig. 7b) shows two well-resolved peaks at 88.8 ppm and 85.7 ppm. Both can be assigned to isolated $[\text{PS}_4]^{3-}$ tetrahedra in the crystal structure⁴⁶, in agreement with the crystal

structure derived from X-ray/neutron diffraction. The fact that two very similar environments are visible in the ^{31}P NMR spectrum although only one site was determined by X-ray/neutron diffraction could hint at small amount of amorphous phase existing. We ascribe the peak at 88.8 ppm to $[\text{PS}_4]^{3-}$ from crystalline $\text{Li}_{15}\text{P}_4\text{S}_{16}\text{Cl}_3$ and peak at 85.7 ppm to amorphous phase, based on the observation that the intensity of peak at 85.7 ppm decreases as heating time is extended and the crystallinity increases.

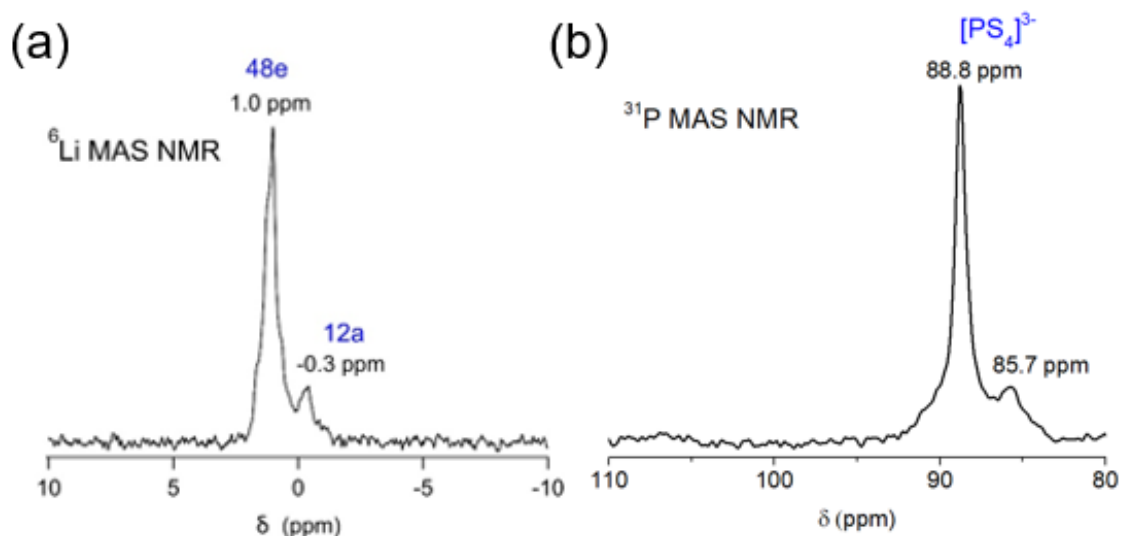


Fig. 7. ^6Li and ^{31}P MAS NMR spectra of $\text{Li}_{15}\text{P}_4\text{S}_{16}\text{Cl}_3$.

The conductivity of $\text{Li}_{15}\text{P}_4\text{S}_{16}\text{Cl}_3$ was measured by electrochemical impedance spectroscopy (EIS). The relative density of the pellet is about 80%, under a uniaxial pressure of 10 MPa. Bulk and grain boundary contributions to the total resistance cannot be deconvoluted (Fig. S2). Fig. 8 shows the temperature dependence of the conductivity of $\text{Li}_{15}\text{P}_4\text{S}_{16}\text{Cl}_3$. $\text{Li}_{15}\text{P}_4\text{S}_{16}\text{Cl}_3$ exhibited a low ionic conductivity of 1.0×10^{-7} S/cm at 30 °C, which is similar to $\beta\text{-Li}_3\text{PS}_4$ (9×10^{-7} S/cm) and $\gamma\text{-Li}_3\text{PS}_4$ (3×10^{-7} S/cm)³. When increasing the temperature to 90 °C, the ionic conductivity reached 3.4×10^{-6} S/cm. The calculated activation energy is 0.57 eV, which is different from $\beta\text{-}$

Li_3PS_4 (0.16 eV) and $\gamma\text{-Li}_3\text{PS}_4$ (0.22 eV). This value is also much higher than those of typical lithium ion conductors such as $\text{Li}_7\text{P}_3\text{S}_{11}$, $\text{Li}_6\text{PS}_5\text{Cl}$ and $\text{Li}_{10}\text{GeP}_2\text{S}_{12}$ ^{21, 25, 50}.

Ab initio molecular dynamics (AIMD) was also used to calculate the theoretical ionic conductivity of this compound. The calculated ionic conductivity is around 10^{-14} S/cm, which is much lower than the experimental results. The conductivity of the sample being much higher than the calculated theoretical value may be caused by the existence of small amount of amorphous impurity phase and defects in the $\text{Li}_{15}\text{P}_4\text{S}_{16}\text{Cl}_3$ material. The amorphous impurity phase may be more conductive than $\text{Li}_{15}\text{P}_4\text{S}_{16}\text{Cl}_3$, which increase the overall measured conductivity. The other reason is that the formation of the impurity could results in slight off-stoichiometry in $\text{Li}_{15}\text{P}_4\text{S}_{16}\text{Cl}_3$, and mobile defects, such as Li vacancies or interstitial Li ions, may exist in $\text{Li}_{15}\text{P}_4\text{S}_{16}\text{Cl}_3$ material, which increases the conductivity. In the AIMD computation, a perfect bulk-phase crystal $\text{Li}_{15}\text{P}_4\text{S}_{16}\text{Cl}_3$ with no pre-existing defects were used, which may

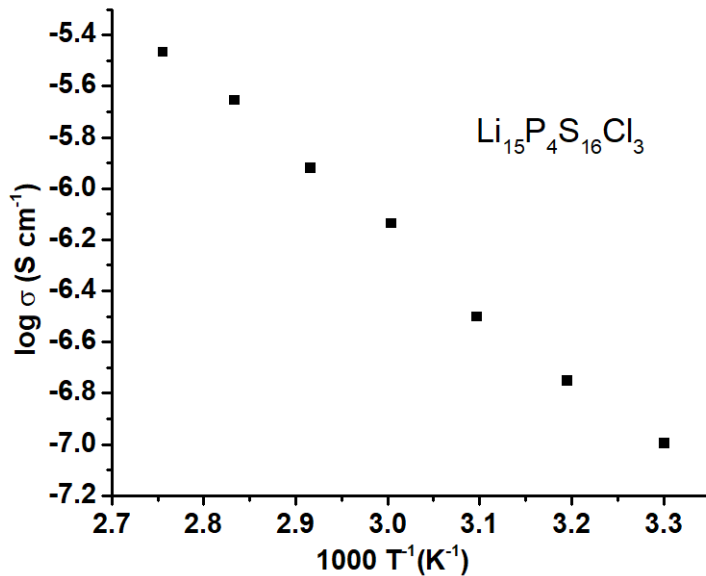


Fig. 8. Arrhenius plot of $\text{Li}_{15}\text{P}_4\text{S}_{16}\text{Cl}_3$. The activation energy is 0.57 eV.

result in a limited carrier concentration for ion conduction. These differences in experiments and computation may have resulted in the differences in conductivity values. The results of the theoretical calculation suggest that lithium ions at both Li(1) and Li(2) sites are involved in the diffusion pathway. The Mean-squared Displacement-time (MSD-t) relationship (Fig. S3) and Li trajectories within 2ps at 1150 K (Fig. 9) indicated that the lithium diffusion path in $\text{Li}_{15}\text{P}_4\text{S}_{16}\text{Cl}_3$ is three-dimensional.

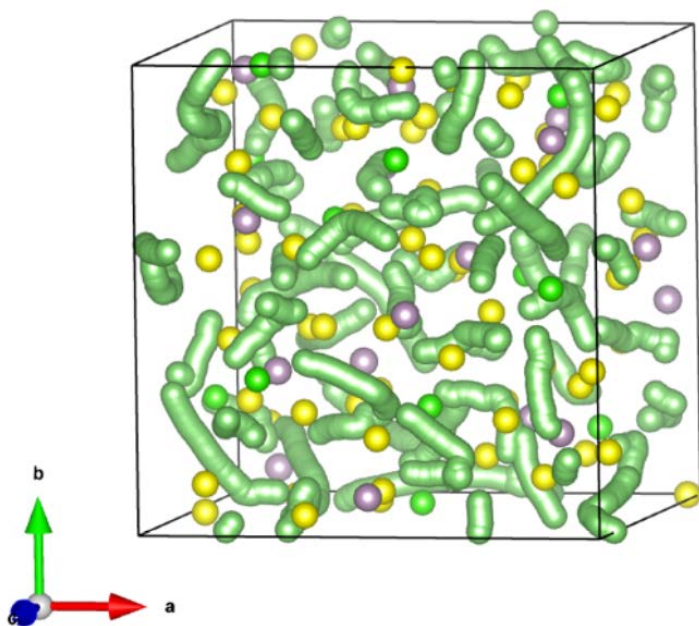


Fig 9. Li trajectories within 2 ps at 1150 K, as obtained from AIMD simulation.

In addition to its ability to investigate local structures element-specifically, solid state NMR is also a powerful tool to probe the dynamics of mobile ions in solids on different time and length scales³⁷. Fig. 10a shows the temperature dependence of static ^7Li NMR spectra of $\text{Li}_{15}\text{P}_4\text{S}_{16}\text{Cl}_3$.

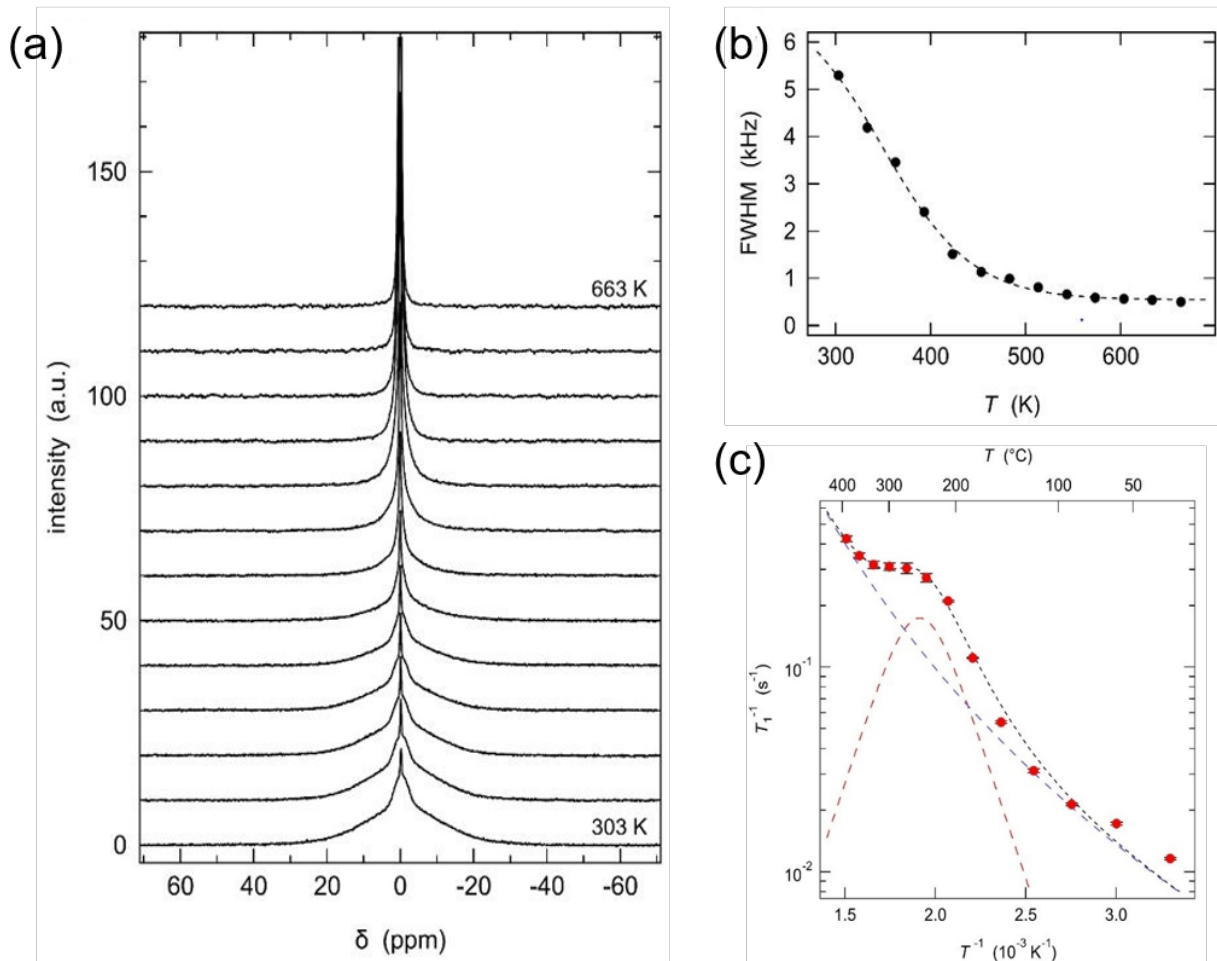


Fig. 10. (a) static ${}^7\text{Li}$ NMR spectra at temperatures between 303 K and 663 K. b) FWHM vs temperature for the broad component in the static ${}^7\text{Li}$ NMR spectra. c) ${}^7\text{Li}$ NMR spin-lattice relaxation rates T_1^{-1} vs inverse temperature.

At low temperatures, the spectra consist of three different contributions, all centered around 0 ppm: (i) a broad contribution in the range from +25 ppm to -25 ppm represents the satellite transitions of the ${}^7\text{Li}$ nuclei (nuclear spin $I = 3/2$), (ii) a narrower signal between +3 ppm and -3 ppm represents the central transition, and (iii) a very narrow component with a width of about 0.5 ppm represents Li ions that are already mobile at these low temperatures. When the temperature

is increased, the broader contributions show a clear so-called motional narrowing. This reflects the temporal averaging of the local environments around the Li ions due the increasingly fast motions of these ions. At 663 K, only a single contribution is visible in the static ^7Li NMR spectrum. The width of the broader component is plotted in Fig. 10b vs temperature. The curve shows no clear plateau at low temperatures and thus reveals that the motional averaging already started well below room temperature. The motion of the Li ions was additionally probed on very short time scales (few nanoseconds) by measuring ^7Li NMR relaxation rates T_1^{-1} as a function of (inverse) temperature (Fig. 10c). A clear maximum, as it was observed for Li_3PS_4 or $\text{Li}_{10}\text{SnP}_2\text{S}_{12}$, could not be observed for $\text{Li}_{15}\text{P}_4\text{S}_{16}\text{Cl}_3$. The relaxation rate rather shows a monotonic increase with increasing temperature and a shoulder at 523 K. The data can be described by a superposition of a diffusion-induced maximum^{37, 51} and a power law contribution (dashed lines in Fig. 10c), which is a commonly used approach to describe such data⁵². The latter one might represent another jump process with a maximum at temperatures too high to be reached in these experiments. The fact that a clear maximum in the overall data is not visible can be ascribed to the quite slow diffusion and thus to a smaller diffusion-induced contribution.

This behavior reveals a quite complex diffusion mechanism involving different jump processes between different Li sites. The diffusion-induced maximum reveals an average hopping rate of the Li ions of about $5 \times 10^8 \text{ s}^{-1}$ at 523 K and an activation barrier for these jumps of $(0.53 \pm 0.06) \text{ eV}$. From the jump rate, a Li ion conductivity of about 10^{-6} S/cm can be extrapolated for 298 K. These values are in good agreement with the EIS results.

Pulsed field gradient (PFG) NMR experiments were performed to study the long-range transport of Li ions, on the time scale of about one second. The echo damping is shown in Fig. 11a for

three different temperatures. As expected, a stronger echo damping is observed with increasing temperature due to faster Li diffusion. The echo damping as a function of gradient field strength

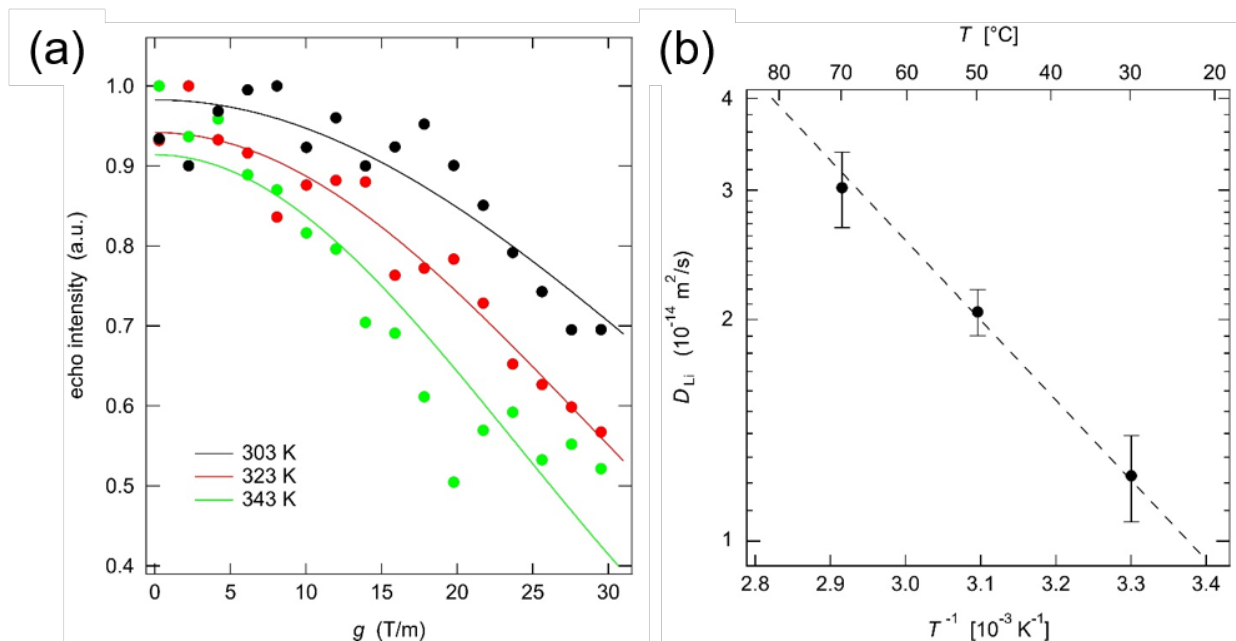


Fig. 11. ⁷Li PFG NMR results on Li₁₅P₄S₁₆Cl₃. a) the echo intensity vs gradient field strength for three different temperatures (gradient duration $\delta = 3$ ms, diffusion time $\Delta = 300$ ms). b) the derived diffusion coefficients vs inverse temperature.

g can be well described with a Gaussian function according to the Sejskal-Tanner equation⁵³ (solid lines in Fig. 11a). The derived diffusion coefficients are displayed in Fig. 11b vs inverse temperature. They show an Arrhenius-type behavior with an activation energy of (0.22 ± 0.04) eV. At 298 K, a diffusion coefficient of 10^{-14} m²/s can be estimated. Assuming an uncorrelated, three-dimensional motion of all Li ions and using the number density of all Li ions (2×10^{28} m⁻³), this would correspond to a Li ion conductivity of 1.3×10^{-5} S/cm, as derived from the Nernst-Einstein equation. This value is higher than the total conductivity measured with impedance

spectroscopy, and also the activation energy derived from PFG NMR is much lower than the 0.57 eV measured with EIS. This might hint at a stronger influence of grain boundaries on the impedance data than on the PFG results that are probing the transport on a time scale of 0.3 s, and thus on a length scale of 0.1 μm . Overall, the NMR results reveal a complex motion of the Li ions involving different types of jump processes, as expected from the crystal structure. The relatively slow dynamics of the Li ions is probably caused by the fully occupied Li(1) and Li(2) sites and the quite dense crystal structure. This provides multiple possibilities for future materials optimization, e.g. via cation and anion doping.

Conclusion

$\text{Li}_{15}\text{P}_4\text{S}_{16}\text{Cl}_3$, a new crystalline thiophosphate was successfully synthesized for the first time. It is a novel quaternary compound in the Li-P-S-Cl system, in addition to argyrodite $\text{Li}_6\text{PS}_5\text{Cl}$. The crystal structure of $\text{Li}_{15}\text{P}_4\text{S}_{16}\text{Cl}_3$ was identified and confirmed by synchrotron XRD and neutron diffraction. Although the room temperature conductivity of this material is low, which may not have practical use in devices that requires high ionic conductivities such as solid state batteries, evidences in both computational predictions and our ongoing follow-up experiments have shown that the conductivity can be drastically improved by cation or anion doping/replacement in this crystal structure, which shows the value of identification of new compound as the motif structure for solid state ionic conductors. The very low formation temperature (<350 $^\circ\text{C}$) and good thermodynamic stability also imply that it can be a good basic structure for design. In fact, we have tried the synthesis of $\text{Li}_{15}\text{P}_4\text{S}_{16}\text{Br}_3$ and $\text{Li}_{15}\text{P}_4\text{S}_{16}\text{I}_3$. $\text{Li}_{15}\text{P}_4\text{S}_{16}\text{Br}_3$ can also be successfully obtained at a lower temperature, implying abundant possibilities of future materials design,

similar to what has been done with argyrodites, which may lead to new ionic conductors with higher conductivity or better stability.

Supporting Information

Crystal structure and Li^+ diffusion properties of $\text{Li}_{15}\text{P}_4\text{S}_{16}\text{Cl}_3$

Acknowledgements

X.H, and Y.M. acknowledge the financial support by acknowledge the support from National Science Foundation under award No. 1550423 and the computational facilities from the University of Maryland supercomputing resources, the Maryland Advanced Research Computing Center (MARCC), and the Extreme Science and Engineering Discovery Environment (XSEDE) supported by National Science Foundation Award No. DMR150038.

Z.L. and H.C. acknowledge the financial support by the U.S. National Science Foundation under grant numbers CBET-1706723 and new faculty startup fund of Georgia Institute of Technology. The use of the Advanced Photon Source and the National Synchrotron Light Source II were supported by the U.S. Department of Energy, Office of Science, through the general user programs. A portion of this research used resources at the Spallation Neutron Source (SNS), a DOE Office of Science User Facility operated by the Oak Ridge National Laboratory.

References

1. Auvergniot, J.; Cassel, A.; Ledeuil, J.-B.; Viallet, V.; Seznec, V.; Dedryvère, R., Interface Stability of Argyrodite $\text{Li}_6\text{PS}_5\text{Cl}$ toward LiCoO_2 , $\text{LiNi}_{1/3}\text{Co}_{1/3}\text{Mn}_{1/3}\text{O}_2$, and LiMn_2O_4 in Bulk All-Solid-State Batteries. *Chemistry of Materials* **2017**, *29* (9), 3883-3890.
2. Auvergniot, J.; Cassel, A.; Foix, D.; Viallet, V.; Seznec, V.; Dedryvère, R., Redox activity of argyrodite $\text{Li}_6\text{PS}_5\text{Cl}$ electrolyte in all-solid-state Li-ion battery: An XPS study. *Solid State Ionics* **2017**, *300* (Supplement C), 78-85.
3. Homma, K.; Yonemura, M.; Kobayashi, T.; Nagao, M.; Hirayama, M.; Kanno, R., Crystal structure and phase transitions of the lithium ionic conductor Li_3PS_4 . *Solid State Ionics* **2011**, *182* (1), 53-58.
4. Murayama, M.; Sonoyama, N.; Yamada, A.; Kanno, R., Material design of new lithium ionic conductor, thio-LISICON, in the $\text{Li}_2\text{S}-\text{P}_2\text{S}_5$ system. *Solid State Ionics* **2004**, *170* (3), 173-180.
5. de Klerk, N. J. J.; Rosłoń, I.; Wagemaker, M., Diffusion Mechanism of Li Argyrodite Solid Electrolytes for Li-Ion Batteries and Prediction of Optimized Halogen Doping: The Effect of Li Vacancies, Halogens, and Halogen Disorder. *Chemistry of Materials* **2016**, *28* (21), 7955-7963.
6. Sedlmaier, S. J.; Indris, S.; Dietrich, C.; Yavuz, M.; Dräger, C.; von Seggern, F.; Sommer, H.; Janek, J., $\text{Li}_4\text{PS}_4\text{I}$: A Li^+ Superionic Conductor Synthesized by a Solvent-Based Soft Chemistry Approach. *Chemistry of Materials* **2017**, *29* (4), 1830-1835.
7. Liu, X.; Chen, Y.; Hood, Z. D.; Ma, C.; Yu, S.; Sharafi, A.; Wang, H.; An, K.; Sakamoto, J.; Siegel, D. J.; Cheng, Y.; Jalarvo, N. H.; Chi, M., Elucidating the mobility of H^+ and Li^+ ions

in $(\text{Li}_{6.25-x}\text{H}_x\text{Al}_{0.25})\text{La}_3\text{Zr}_2\text{O}_{12}$ via correlative neutron and electron spectroscopy. *Energy & Environmental Science* **2019**.

8. Hood, Z. D.; Wang, H.; Samuthira Pandian, A.; Keum, J. K.; Liang, C., Li_2OHCl Crystalline Electrolyte for Stable Metallic Lithium Anodes. *Journal of the American Chemical Society* **2016**, *138* (6), 1768-1771.
9. Deng, Y.; Eames, C.; Nguyen, L. H. B.; Pecher, O.; Griffith, K. J.; Courty, M.; Fleutot, B.; Chotard, J.-N.; Grey, C. P.; Islam, M. S.; Masquelier, C., Crystal Structures, Local Atomic Environments, and Ion Diffusion Mechanisms of Scandium-Substituted Sodium Superionic Conductor (NASICON) Solid Electrolytes. *Chemistry of Materials* **2018**, *30* (8), 2618-2630.
10. Suzuki, N.; Richards, W. D.; Wang, Y.; Miara, L. J.; Kim, J. C.; Jung, I.-S.; Tsujimura, T.; Ceder, G., Synthesis and Electrochemical Properties of $\text{I}^{\bar{4}}$ -Type $\text{Li}_{1+2x}\text{Zn}_{1-x}\text{PS}_4$ Solid Electrolyte. *Chemistry of Materials* **2018**, *30* (7), 2236-2244.
11. Kaup, K.; Lalère, F.; Huq, A.; Shyamsunder, A.; Adermann, T.; Hartmann, P.; Nazar, L. F., Correlation of Structure and Fast Ion Conductivity in the Solid Solution Series $\text{Li}_{1+2x}\text{Zn}_{1-x}\text{PS}_4$. *Chemistry of Materials* **2018**, *30* (3), 592-596.
12. Aihara, Y.; Ito, S.; Omoda, R.; Yamada, T.; Fujiki, S.; Watanabe, T.; Park, Y.; Doo, S., The Electrochemical Characteristics and Applicability of an Amorphous Sulfide-Based Solid Ion Conductor for the Next-Generation Solid-State Lithium Secondary Batteries. *Frontiers in Energy Research* **2016**, *4* (18).
13. Miara, L.; Windmüller, A.; Tsai, C.-L.; Richards, W. D.; Ma, Q.; Uhlenbruck, S.; Guillon, O.; Ceder, G., About the Compatibility between High Voltage Spinel Cathode Materials and Solid Oxide Electrolytes as a Function of Temperature. *ACS Applied Materials & Interfaces* **2016**, *8* (40), 26842-26850.

14. Uhlenbruck, S.; Dornseiffer, J.; Lobe, S.; Dellen, C.; Tsai, C.-L.; Gotzen, B.; Sebold, D.; Finsterbusch, M.; Guillon, O., Cathode-electrolyte material interactions during manufacturing of inorganic solid-state lithium batteries. *Journal of Electroceramics* **2017**, *38* (2), 197-206.
15. Hayashi, A.; Sakuda, A.; Tatsumisago, M., Development of Sulfide Solid Electrolytes and Interface Formation Processes for Bulk-Type All-Solid-State Li and Na Batteries. *Frontiers in Energy Research* **2016**, *4* (25).
16. Knauth, P., Inorganic solid Li ion conductors: An overview. *Solid State Ionics* **2009**, *180* (14), 911-916.
17. Park, K. H.; Bai, Q.; Kim, D. H.; Oh, D. Y.; Zhu, Y.; Mo, Y.; Jung, Y. S., Design Strategies, Practical Considerations, and New Solution Processes of Sulfide Solid Electrolytes for All-Solid-State Batteries. *Advanced Energy Materials* **2018**, *8* (18), 1800035.
18. Xiong, S.; Liu, Z.; Rong, H.; Wang, H.; McDaniel, M.; Chen, H., Na₃SbSe_{4-x}S_x as Sodium Superionic Conductors. *Scientific Reports* **2018**, *8* (1), 9146.
19. Kanno, R.; Murayama, M., Lithium Ionic Conductor Thio-LISICON: The Li₂S-GeS₂-P₂S₅ System. *Journal of The Electrochemical Society* **2001**, *148* (7), A742-A746.
20. Yu, C.; Ganapathy, S.; van Eck, E. R. H.; van Eijck, L.; Basak, S.; Liu, Y.; Zhang, L.; Zandbergen, H.; Wagemaker, M., Revealing the relation between the structure, Li-ion conductivity and solid-state battery performance of the argyrodite Li₆PS₅Br solid electrolyte. *Journal of Materials Chemistry A* **2017**.
21. Deiseroth, H.-J.; Maier, J.; Weichert, K.; Nickel, V.; Kong, S.-T.; Reiner, C., Li₇PS₆ and Li₆PS₅X (X: Cl, Br, I): Possible Three-dimensional Diffusion Pathways for Lithium Ions and Temperature Dependence of the Ionic Conductivity by Impedance Measurements. *Zeitschrift für anorganische und allgemeine Chemie* **2011**, *637* (10), 1287-1294.

22. Rao, R. P.; Adams, S., Studies of lithium argyrodite solid electrolytes for all-solid-state batteries. *physica status solidi (a)* **2011**, *208* (8), 1804-1807.
23. Ziolkowska, D. A.; Arnold, W.; Druffel, T.; Sunkara, M.; Wang, H., Rapid and Economic Synthesis of a Li_7PS_6 Solid Electrolyte from a Liquid Approach. *ACS Applied Materials & Interfaces* **2019**, *11* (6), 6015-6021.
24. Yamane, H.; Shibata, M.; Shimane, Y.; Junke, T.; Seino, Y.; Adams, S.; Minami, K.; Hayashi, A.; Tatsumisago, M., Crystal structure of a superionic conductor, $\text{Li}_7\text{P}_3\text{S}_{11}$. *Solid State Ionics* **2007**, *178* (15), 1163-1167.
25. Kamaya, N.; Homma, K.; Yamakawa, Y.; Hirayama, M.; Kanno, R.; Yonemura, M.; Kamiyama, T.; Kato, Y.; Hama, S.; Kawamoto, K.; Mitsui, A., A lithium superionic conductor. *Nat Mater* **2011**, *10* (9), 682-686.
26. Brant, J. A.; Massi, D. M.; Holzwarth, N. A. W.; MacNeil, J. H.; Douvalis, A. P.; Bakas, T.; Martin, S. W.; Gross, M. D.; Aitken, J. A., Fast Lithium Ion Conduction in Li_2SnS_3 : Synthesis, Physicochemical Characterization, and Electronic Structure. *Chemistry of Materials* **2015**, *27* (1), 189-196.
27. Kraft, M. A.; Culver, S. P.; Calderon, M.; Böcher, F.; Krauskopf, T.; Senyshyn, A.; Dietrich, C.; Zevalkink, A.; Janek, J.; Zeier, W. G., Influence of Lattice Polarizability on the Ionic Conductivity in the Lithium Superionic Argyrodites $\text{Li}_6\text{PS}_5\text{X}$ (X = Cl, Br, I). *Journal of the American Chemical Society* **2017**, *139* (31), 10909-10918.
28. Kraft, M. A.; Ohno, S.; Zinkevich, T.; Koerver, R.; Culver, S. P.; Fuchs, T.; Senyshyn, A.; Indris, S.; Morgan, B. J.; Zeier, W. G., Inducing High Ionic Conductivity in the Lithium Superionic Argyrodites $\text{Li}_{6+x}\text{P}_{1-x}\text{Ge}_x\text{S}_5\text{I}$ for All-Solid-State Batteries. *Journal of the American Chemical Society* **2018**, *140* (47), 16330-16339.

29. Zhu, Z.; Chu, I.-H.; Ong, S. P., $\text{Li}_3\text{Y}(\text{PS}_4)_2$ and $\text{Li}_5\text{PS}_4\text{Cl}_2$: New Lithium Superionic Conductors Predicted from Silver Thiophosphates using Efficiently Tiered Ab Initio Molecular Dynamics Simulations. *Chemistry of Materials* **2017**, *29* (6), 2474-2484.
30. Haomin, C. Computational design of inorganic ionic conductors. Thesis, National University of Singapore, ScholarBank@NUS Repository, 2017.
31. Toby, B. H.; Von Dreele, R. B., GSAS-II: the genesis of a modern open-source all purpose crystallography software package. *Journal of Applied Crystallography* **2013**, *46* (2), 544-549.
32. Perl, J.; Shin, J.; Schümann, J.; Faddegon, B.; Paganetti, H., TOPAS: An innovative proton Monte Carlo platform for research and clinical applications. *Medical Physics* **2012**, *39* (11), 6818-6837.
33. Juhas, P.; Davis, T.; Farrow, C. L.; Billinge, S. J. L., PDFgetX3: a rapid and highly automatable program for processing powder diffraction data into total scattering pair distribution functions. *Journal of Applied Crystallography* **2013**, *46* (2), 560-566.
34. Farrow, C. L.; Juhas, P.; Liu, J. W.; Bryndin, D.; Božin, E. S.; Bloch, J.; Th, P.; Billinge, S. J. L., PDFfit2 and PDFgui: computer programs for studying nanostructure in crystals. *Journal of Physics: Condensed Matter* **2007**, *19* (33), 335219.
35. Duer, M. J., *Introduction to Solid-State NMR Spectroscopy*. Blackwell Publishing: Oxford: 2004.
36. Fukushima, E.; Roeder, S. B. W., *Experimental Pulse NMR – A Nuts and Bolts Approach*. Addison-Wesley: Reading: 1981.
37. Paul Heitjans; Sylvio Indris; Wilkening, M., Solid-State Diffusion and NMR. *Diffusion Fundamentals* **2005**, *2* (45), 1-20.

38. Price, W. S., Pulsed-field gradient nuclear magnetic resonance as a tool for studying translational diffusion: Part 1. Basic theory. *Concepts in Magnetic Resonance* **1997**, 9 (5), 299-336.
39. Kresse, G.; Furthmuller, J., Efficient iterative schemes for ab initio total-energy calculations using a plane-wave basis set. *Phys. Rev. B.* **1996**, 54 (16), 11169–11186.
40. Perdew, J. P.; Ernzerhof, M.; Burke, K., Rationale for mixing exact exchange with density functional approximations. *J. Chem. Phys.* **1996**, 105 (22), 9982–9985.
41. Nose, S., Constant temperature molecular dynamics methods. *Prog. Theor. Phys. Suppl.* **1991**, 103, 1–46.
42. He, X.; Zhu, Y.; Epstein, A.; Mo, Y., Statistical variances of diffusional properties from ab initio molecular dynamics simulations. *npj Computational Materials* **2018**, 4 (1), 18.
43. Wang, Y.; Lu, D.; Bowden, M.; El Khoury, P. Z.; Han, K. S.; Deng, Z. D.; Xiao, J.; Zhang, J.-G.; Liu, J., Mechanism of Formation of Li₇P₃S₁₁ Solid Electrolytes through Liquid Phase Synthesis. *Chemistry of Materials* **2018**, 30 (3), 990-997.
44. Holzwarth, N. A. W.; Lepley, N. D.; Du, Y. A., Computer modeling of lithium phosphate and thiophosphate electrolyte materials. *Journal of Power Sources* **2011**, 196 (16), 6870-6876.
45. Deng, Z.; Zhu, Z.; Chu, I.-H.; Ong, S. P., Data-Driven First-Principles Methods for the Study and Design of Alkali Superionic Conductors. *Chemistry of Materials* **2017**, 29 (1), 281-288.
46. Dietrich, C.; Weber, D. A.; Culver, S.; Senyshyn, A.; Sedlmaier, S. J.; Indris, S.; Janek, J.; Zeier, W. G., Synthesis, Structural Characterization, and Lithium Ion Conductivity of the Lithium Thiophosphate Li₂P₂S₆. *Inorganic Chemistry* **2017**, 56 (11), 6681-6687.

47. Dietrich, C.; Sadowski, M.; Sicolo, S.; Weber, D. A.; Sedlmaier, S. J.; Weldert, K. S.; Indris, S.; Albe, K.; Janek, J.; Zeier, W. G., Local Structural Investigations, Defect Formation, and Ionic Conductivity of the Lithium Ionic Conductor Li₄P₂S₆. *Chemistry of Materials* **2016**, *28* (23), 8764-8773.
48. Jörgens, S.; Mewis, A., Ag₅PS₄Cl₂ and Ag₁₅(PS₄)₄Cl₃ – Crystal structures and their relation to Ag₃PS₄. *Solid State Sciences* **2007**, *9* (2), 213-217.
49. Shannon, R., Revised effective ionic radii and systematic studies of interatomic distances in halides and chalcogenides. *Acta Crystallographica Section A* **1976**, *32* (5), 751-767.
50. Seino, Y.; Ota, T.; Takada, K.; Hayashi, A.; Tatsumisago, M., A sulphide lithium super ion conductor is superior to liquid ion conductors for use in rechargeable batteries. *Energy & Environmental Science* **2014**, *7* (2), 627-631.
51. Vinod Chandran, C.; Pristat, S.; Witt, E.; Tietz, F.; Heitjans, P., Solid-State NMR Investigations on the Structure and Dynamics of the Ionic Conductor Li_{1+x}Al_xTi_{2-x}(PO₄)₃ (0.0 ≤ x ≤ 1.0). *The Journal of Physical Chemistry C* **2016**, *120* (16), 8436-8442.
52. Wilkening, M.; Heitjans, P., Li jump process in h-Li_{0.7}TiS₂ studied by two-time ⁷Li spin-alignment echo NMR and comparison with results on two-dimensional diffusion from nuclear magnetic relaxation. *Physical Review B* **2008**, *77* (2), 024311.
53. Stejskal, E. O.; Tanner, J. E., Spin Diffusion Measurements: Spin Echoes in the Presence of a Time-Dependent Field Gradient. *The Journal of Chemical Physics* **1965**, *42* (1), 288-292.

Supporting Information for: $\text{Li}_{15}\text{P}_4\text{S}_{16}\text{Cl}_3$, a new lithium chloro-thiophosphate as a solid-state ionic conductor

Zhantao Liu¹, Tatiana Zinkevich², Sylvio Indris², Xingfeng He³, Jue Liu⁴, Wenqian Xu⁵, Jianming Bai⁶, Shan Xiong¹, Yifei Mo³, Hailong Chen^{1*}

¹ *The Woodruff School of Mechanical Engineering, Georgia Institute of Technology, Atlanta, GA, 30332, USA*

² *Institute for Applied Materials, Karlsruhe Institute of Technology, Hermann-von-Helmholtz Platz 1, D-76344 Eggenstein-Leopoldshafen, Germany*

³ *Department of Materials Science and Engineering, University of Maryland, College Park, Maryland 20742, USA*

⁴ *Neutron Scattering Division, Oak Ridge National Laboratory, Oak Ridge, Tennessee 37831, United States*

⁵ *X-ray Science Division, Advanced Photon Source, Argonne National laboratory, Argonne, Illinois 60439, United States*

⁶ *National Synchrotron Light Source II, Brookhaven National Laboratory, Upton, New York 11973, United States*

Correspondence should be addressed to Hailong Chen via E-mail address: hailong.chen@me.gatech.edu

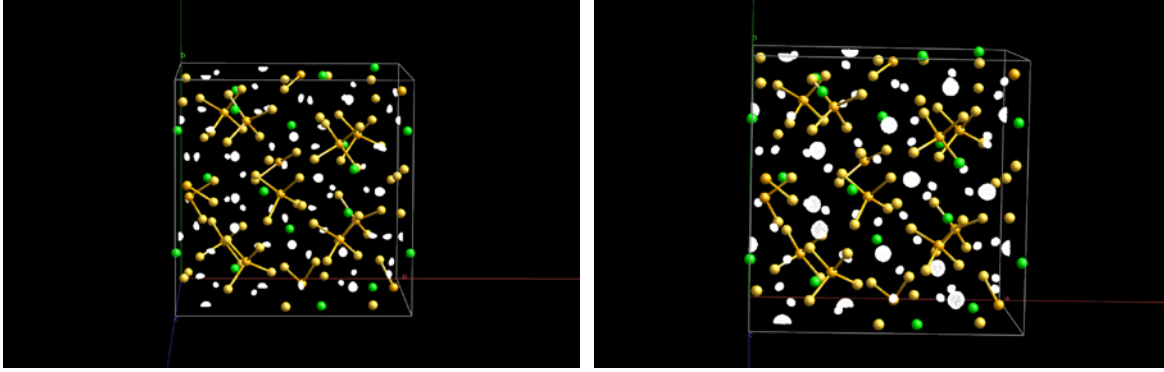


Figure S1. Difference Fourier maps used to identify Li sites generated from synchrotron X-ray diffraction data (left, where white regions indicate positive difference peaks associated with the Li electron density) and time-of-flight neutron diffraction data (right, where white regions indicate negative peaks associated with the Li coherent nuclear scattering length density). The residual positions from both X-ray diffraction and neutron diffraction matches well with the refined positions from Rietveld refinement.

Table S1. Refined structure of $\text{Li}_{15}\text{P}_4\text{S}_{16}\text{Cl}_3$ using synchrotron diffraction data ($\lambda = 0.24116 \text{ \AA}$).

| S.G. $I-43d$ $a = 14.3066(4) \text{ \AA}$ | | | | | | |
|---|-------|------------|------------|------------|------|---------------------------------|
| Site | Wyck. | x | y | z | Occ. | $B_{\text{iso}} (\text{\AA}^2)$ |
| Li(1) | 12a | 0.00000 | 0.25000 | 0.37500 | 1 | 3.65(48) |
| Li(2) | 48e | 0.1427(13) | 0.2082(15) | 0.5921(19) | 1 | 3.65(48) |
| S(1) | 16c | 0.0322(2) | 0.0322(2) | 0.0322(2) | 1 | 1.35(7) |
| S(2) | 48e | 0.1086(2) | 0.3428(3) | 0.4721(2) | 1 | 1.35(7) |
| Cl(1) | 12b | 0.00000 | 0.25000 | 0.87500 | 1 | 2.23(17) |
| P(1) | 16c | 0.1996(2) | 0.1996(2) | 0.1996(2) | 1 | 1.18(13) |

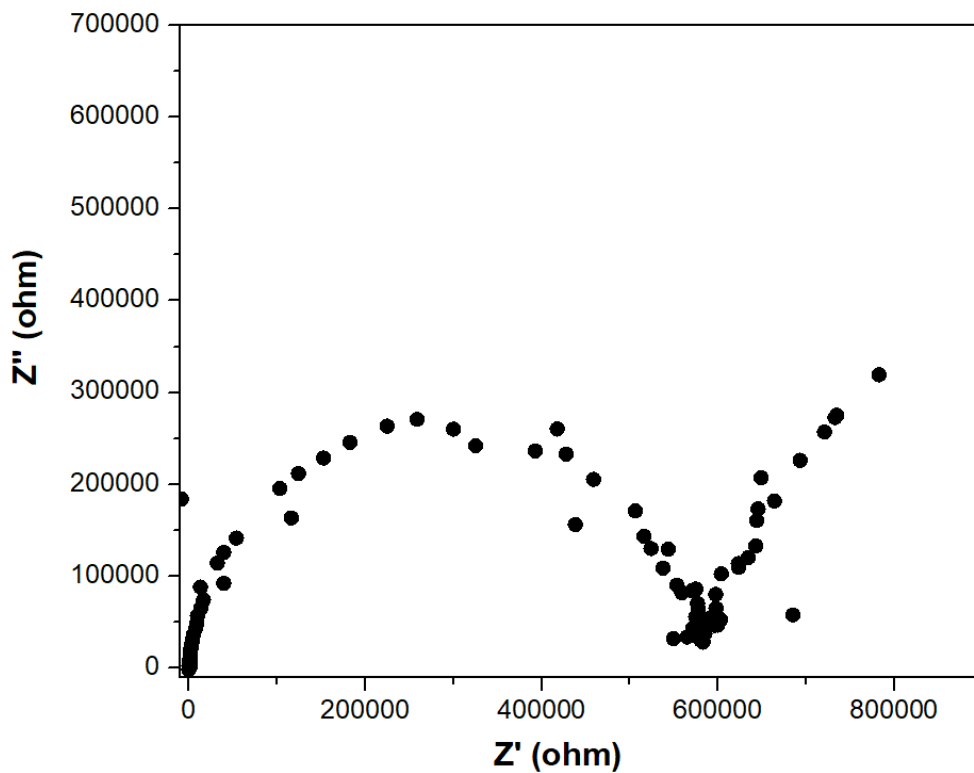


Fig. S2. Nyquist plot of $\text{Li}_{15}\text{P}_4\text{S}_{16}\text{Cl}_3$ at 30 °C.

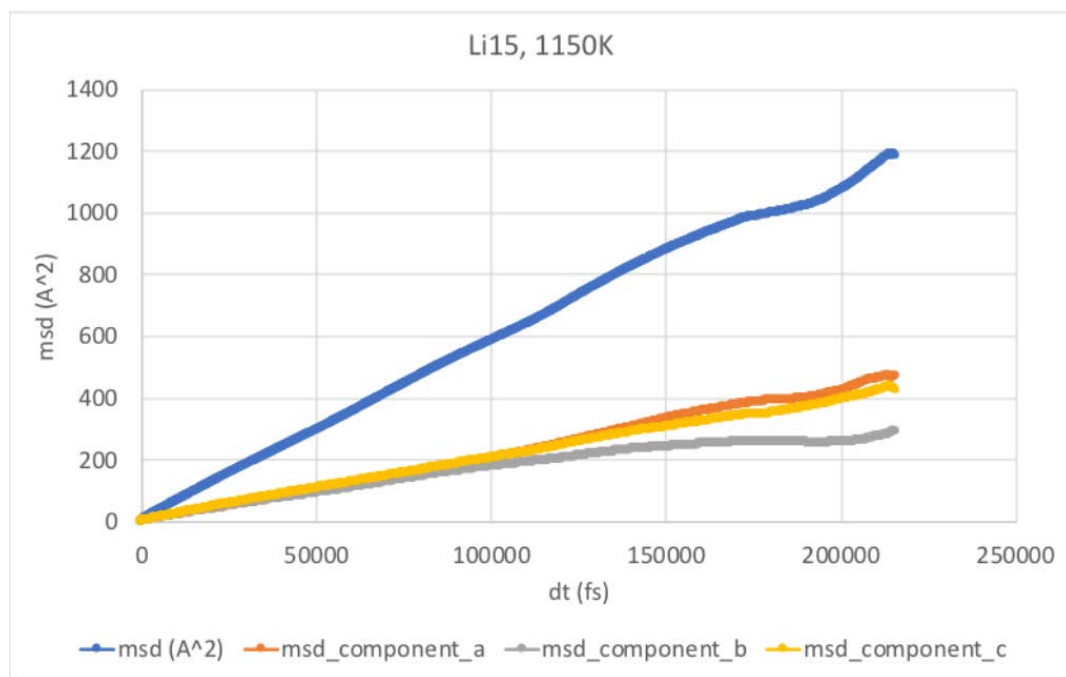


Fig. S3. The Mean-squared Displacement-time (MSD-t) relationship